Catalysis Science & Technology

ROYAL SOCIETY OF CHEMISTRY

PAPER

View Article Online
View Journal | View Issue

Cite this: *Catal. Sci. Technol.*, 2025, 15, 3412

Vacancy formation, stability, and electronic properties of nickel on equimolar ceria–zirconia mixed oxide (111) catalyst†

Sanjana Srinivas, [ab] George Yan, [b] Stavros Caratzoulas[b] and Dionisios G. Vlachos *[ab]

Received 4th February 2025,
Accepted 17th April 2025

DOI: 10.1039/d5cy00133a

rsc.li/catalysis

Nickel (Ni) single atoms and small clusters dispersed on $Ce_{0.5}Zr_{0.5}O_2$ (CZO) are promising for the dry reforming of methane (DRM). However, understanding of defects and electronic interactions between Ni motifs and (non) stoichiometric CZO surfaces is limited. Here, we use Density Functional Theory (DFT) and *ab initio* thermodynamics to investigate vacancy formation and electronic properties of Ni_1 and Ni_4 on CZO(111). Surface and subsurface oxygen vacancies near Zr^{4+} ions dominate due to distortion-induced stabilization across DRM-relevant chemical potentials; vacancies prefer to be subsurface. Interestingly, Ni single atoms coordinate with two O_{Zr} surface atoms on CZO(111) (Ni_{Ce_2Zr}), unlike three-fold coordinated Ni atoms on hollow sites of CeO_2(111). Ni_1 does not directly bind to oxygen vacancies due to its oxophilicity and steric hindrance caused by multiple surface Ce^{3+} ions. Clusters, on the other hand, can bind favorably at a surface oxygen vacancy. Ni adatoms are more stable than Ni_4 at trimer defects comprising one Ce and two oxygen vacancies ($Ce_v(O_v)_2$), at the pristine surface, and at the Ni_{Ce_2Zr} site with a next-nearest neighbor oxygen vacancy due to coordination with more oxygen atoms. The extent of electron transfer from the metal to the surface and, thus, the degree of cationic character of a nickel adatom varies with its location and defect type and correlate positively with its resistance to sintering. We discuss the expected heterogeneity of actual catalysts.

Introduction

The recent shale gas boom in the US,[1] the growing need to reduce carbon emissions, and the importance of hydrogen in transitioning to a renewable energy economy[2,3] make the dry reforming of methane (DRM) ($CH_4 + CO_2 \leftrightarrow 2H_2 + 2CO$) an attractive route to produce hydrogen. Reducible metal oxides are potential catalyst supports as they allow facile oxygen vacancy formation and replenishment in the Mars–van Krevelen-type mechanism. CeO_2 and mixed CeO_2–ZrO_2 oxides ($Ce_xZr_{1-x}O_2$) have been shown to be excellent supports for this reaction,[4] owing to their high oxygen storage capacity (OSC). Liu *et al.*[5] have shown that $Ce_xZr_{1-x}O_2$ is easier to reduce because Zr is smaller than Ce, which introduces lattice distortions and weakens the Ce–O bonds.[6,7] Homogeneously dispersed Zr^{4+} in the CeO_2 lattice at a Ce : Zr ratio of 1 : 1 (hereafter referred to as CZO) shows the highest reducibility and OSC.[7,8]

Highly dispersed nickel on CZO is an attractive catalyst for DRM because of nickel's abundance, high activity, and resistance to coking.[9–11] The complex electronic structure of this catalyst remains largely unexplored. Different defects (*e.g.*, oxygen and/or cerium vacancies) can be stabilized during DRM's reduction and oxidation half cycles, but the dominant defect configurations and their distribution are unknown. The nuclearity of Ni clusters could influence the relative stability of defects with potential ramifications for catalysis, but a practical catalyst will often contain a broad distribution of Ni cluster nuclearities. These complexities ultimately hinder a detailed mechanistic understanding, as the interpretation of spectroscopic data for detecting defect-Ni interactions hinges on the structural homogeneity of the catalyst. Furthermore, state-of-the-art experimental techniques have yielded limited information about the active site and its local coordination.[12,13] First-principles simulations could provide insights into the physicochemical interactions at the atomic scale.

To shed light on the structure of Ni/CZO catalysts, we use density functional theory (DFT) to electronically characterize vacancy formation as well as nickel adsorption on pristine

[a] *Department of Chemical and Biomolecular Engineering, University of Delaware, 150 Academy St., Newark, DE 19716, USA. E-mail: vlachos@udel.edu*
[b] *Delaware Energy Institute, University of Delaware, 221 Academy St., Newark, DE 19716, USA*

† Electronic supplementary information (ESI) available. See DOI: https://doi.org/10.1039/d5cy00133a

and defected CZO surfaces. By evaluating the vacancy formation and nickel adsorption energies, we gain insights into the relative stability of the nickel single atom and clusters on different surfaces. This paper is organized as follows: first, we identify the location and configuration of stable oxygen vacancies on the CZO(111) surface, then we investigate the possibility of cerium vacancies and discuss the electronic and geometric properties of defected surfaces. To predict surface structure under experimentally relevant environments, we investigate the stability of different defects at finite temperatures and varying oxygen partial pressure. Next, we assess the stability of a Ni adatom and Ni_4 cluster on stoichiometric and non-stoichiometric CZO(111) and vacancy formation in the presence of nickel and provide insights into nickel–support electronic interactions. Last, we discuss the interplay between Ni binding and vacancy formation under different oxygen conditions.

Methodology

Periodic electronic structure calculations

All electronic structure calculations were performed within the spin-polarized DFT framework, using the Vienna *ab initio* simulation package (VASP),[14,15] version 5.4.1. The exchange–correlation energy was calculated using the Perdew–Burke–Ernzerhof (PBE)[16] functional within the generalized gradient approximation (GGA). The core electrons of each atom were described by the projector-augmented wave function (PAW)[17,18] method, and the VASP-recommended pseudopotentials (v54) were used for all elements. The one-electron wave functions were developed on a plane-wave basis set with an energy cutoff of 500 eV. The Ce 4f, 5s, 5p, 5d, and 6s electrons; the O 2s and 2p electrons; the Ni 3d and 4s electrons; and the Zr 4s, 4p, 4d, and 5s electrons were treated as valence electrons. The Brillouin zone was sampled at the gamma point. A maximum force convergence criterion of 0.05 eV $Å^{-1}$ was used, and each self-consistency loop was iterated until reaching a convergence level of 10^{-6} eV. It is well known that the GGA method incorrectly reproduces the band gaps of CeO_2 and ZrO_2 and fails to accurately describe the localization of Ce 4f states upon oxygen vacancy formation in CeO_2, on account of the electrons being strongly correlated in the Ce 4f state. To remedy this, we adopt the DFT+U formalism,[19,20] which has been extensively benchmarked and shown great success in describing vacancy formation, dopant behavior, and catalytic activity on CeO_2. Informed by the vast literature on CeO_2 and less so on ZrO_2, we select U = 5 eV for the Ce 4f states[21] and U = 4 eV for the Zr 4d states.[22] Similar to the approach presented by Livraghi *et al.*,[23] our work also employs the DFT+U formalism for Zr in CZO, as GGA functionals incorrectly reproduce the bandgap for early transition metal oxides like ZrO_2. For comparison, we compute the surface and subsurface vacancy formation energy on a p(4 × 4) CeO_2(111) surface and the bulk vacancy formation energy in a (2 × 2 × 2) supercell of bulk CeO_2 to ensure similar oxygen vacancy concentrations, using the same settings. Since multiple local minima with different Ce^{3+} configurations can exist upon reduction or nickel adsorption, we explored the thermodynamically preferred arrangements of Ce^{3+} sites, focusing on those nearest and next-nearest to the adsorbed nickel species. To generate these configurations, we employed a two-step structural optimization: we first biased the reduction by substituting the target Ce atoms with La, followed by restoring Ce and performing a final relaxation to obtain the desired Ce^{3+} configuration.[24]

Bulk and surface models of CZO

Two types of bulk phases are often considered in modeling CZO: the κ-$Ce_2Zr_2O_8$ phase, which has segregated blocks of CeO_2 and ZrO_2 units as viewed along [001], and the t-$Ce_2Zr_2O_8$ phase, which has uniformly distributed Ce^{4+} and Zr^{4+} ions, as viewed along [001]. The high OSC of the κ-$Ce_2Zr_2O_8$ phase with its electronic and geometric origins has been widely studied by DFT.[25,26] While segregation has been suggested at high temperatures under oxidizing/reducing environments by EXAFS studies,[8,27] its extent, dependence on the environment and temperature, and the synthesis procedure remain elusive. Computational studies of bulk CZO have shown low energy gains from phase segregation compared to the random cation arrangement, which can exhibit multiple local minima.[28] Therefore, in this work, we assume uniform ordering of Ce^{4+} and Zr^{4+} cations in bulk and investigate surfaces cut from the less studied t-phase. To model the CZO unit cell, we substitute Zr atoms for two Ce atoms in the unit cell of cubic-fluorite CeO_2. The bulk structure, which is a (2 × 2 × 2) supercell of the cubic unit cell is shown in Fig. S1.† Bulk oxygen vacancy formation energies are computed using this structure. The structure is only slightly distorted from the cubic fluorite to a tetragonal geometry (c/a = 1.005),[28] resulting in uniform surface cuts.

From the aforementioned bulk structure, we carved out the perfect crystal's most stable (111) and (110) surfaces. We constructed a 9-layer slab (3 O–Ce–O tri-layers) with the 3rd tri-layer frozen during optimization for the (111) surface and a 6-layer slab with the bottom two layers fixed during optimization for the (110) surface. For both surfaces, we used a p(2 × 2) slab and a 20 Å thick vacuum layer. The (111) surface is 10.2 J m^{-2} more stable than the (110), like in stoichiometric CeO_2.[29] The lower energy of the (111) termination can be attributed to the Ce and Zr atoms each having one less bond with lattice O (7-coordinate surface atoms) whereas, on the (110) surface, each metal atom has two less bonds with O (6-coordinate surface atoms) (Fig. S2†). All subsequent analysis on vacancy formation and Ni adsorption was done on the (111) surface. The top-view of the CZO(111) surface is shown in Fig. 1a.

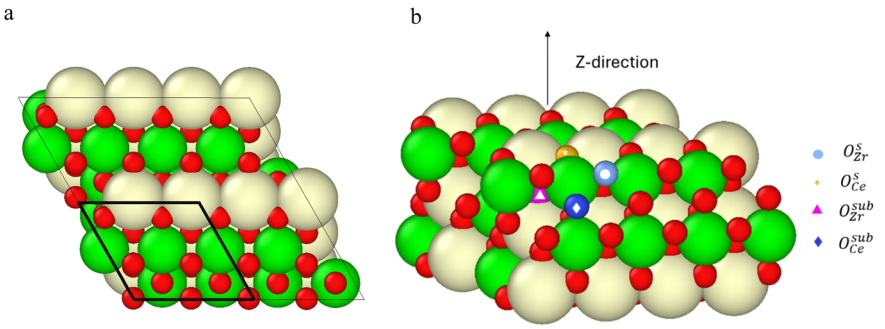

Fig. 1 (a) Top-view of the p(2 × 2) CZO(111) surface, and (b) CZO(111) surface showing the four types of oxygen atoms involved in vacancy formation. (O, red; Ce, yellow; Zr, green).

Results and discussion

Formation, structure, and stability of O and Ce vacancies without Ni

The (111) surface of CZO has two types of surface O atoms: O coordinated to two Ce and one Zr atom (hereafter O^{s}_{Ce}), and O coordinated to two Zr and one Ce atom (hereafter O^{s}_{Zr}). The subsurface O atoms are coordinated to two Ce and two Zr atoms; three atoms lie in the same tri-layer as the oxygen, and one in the layer below it. Therefore, subsurface oxygens are of two types as well: one, where the same tri-layer atoms comprise two Ce and one Zr atom (hereafter O^{sub}_{Ce}) and the other with two Zr and one Ce atom in the same layer (hereafter O^{sub}_{Zr}). The bulk oxygen atoms are uniform. Fig. 1b shows the types of oxygen atoms. Visual inspection shows that the O^{sub}_{Zr} and O^{s}_{Zr} atoms are displaced downward along the surface-normal compared to the O^{sub}_{Ce} and O^{s}_{Ce} atoms (Table S1†), resulting in elongated Ce–O_{Zr} bonds (by ~0.06 Å).

Assuming a neutral oxygen vacancy ($O^{\times}_{O} \rightarrow \frac{1}{2}O_2 + V^{\times}_{O}$, in Kröger–Vink notation), its formation energy is independent of the Fermi level and given by eqn (1)

$$\Delta E^{O_v} = E^{O_v\text{-CZO}} + \frac{1}{2}E_{O_2} - E^{\text{s-CZO}} \quad (1)$$

where $E^{\text{s-CZO}}$ is the total energy of the stoichiometric CZO slab (s-CZO referring to the stoichiometric CZO surface), $E^{O_v\text{-CZO}}$ is the total energy of the CZO slab with an oxygen vacancy (vacancy coverage Θ = 1/16), and E_{O_2} is the energy of a gas-phase O_2 molecule. Table 1 shows ΔE^{O_v} for the five defect sites at O^{s}_{Ce}, O^{s}_{Zr}, O^{sub}_{Ce}, O^{sub}_{Zr}, and O^{b}_{Ce} = O^{b}_{Zr} in CZO(111), and the three defect sites at O^{s}, O^{sub} and O^{b} in CeO_2(111), for comparison.

Table 1 Oxygen vacancy formation energy for CZO(111) and CeO_2(111)

ΔE^{O_v} (eV)	O_{Ce}–CZO	O_{Zr}–CZO	O–CeO_2
Bulk	2.69	2.69	2.79
Subsurface	1.81	1.22	1.98
Surface	2.06	1.42	2.02

Energetically speaking, O_{Zr} vacancies are easier to form than O_{Ce} vacancies on both the surface and subsurface (Table 1). Among the O_{Zr} vacancies, the subsurface O vacancies are more stable than those on the surface, and the bulk vacancies are the least stable, similar to what has been observed for CeO_2(111).[30] Comparing the oxygen vacancy formation energies in Table 1, Zr doping clearly facilitates their formation in CZO(111) compared to CeO_2(111). The preference of an oxygen vacancy in the subsurface near a Zr cation has been reported previously on Zr-doped CeO_2(111) surfaces.[31] The relative stability trends between O_{Zr} and O_{Ce} vacancies remain the same across different U values for the Ce f-orbitals (Table S2†).

Next, we consider the energetics for cerium vacancy formation on CZO(111) and compare with previous studies of cerium vacancies on CeO_2(111), particularly their interactions with Au and Ir single atoms,[21,32] as well as with the Ni-substituted surface examined in this work. Assuming a neutral defect ($Ce^{\times}_{Ce} + O_2 \rightarrow CeO_2(s) + V^{\times}_{Ce}$), its formation energy is given by eqn (2)

$$\Delta E^{Ce_v} = E^{Ce_v\text{-CZO}} + e^{\text{bulk}}_{CeO_2} - E_{O_2} - E^{\text{s-CZO}} \quad (2)$$

where $E^{\text{s-CZO}}$ and E_{O_2} were defined earlier, $E^{Ce_v\text{-CZO}}$ is the total energy of the slab with a Ce vacancy, and $e^{\text{bulk}}_{CeO_2}$ is the total energy of bulk ceria per chemical formula. With ΔE^{Ce_v} = 4.1 eV, $V^{\times}_{Ce}$ formation in CZO(111) is more facile than in undoped CeO_2(111) by 0.6 eV but still unlikely compared to oxygen vacancy formation.

The data raises the question: how does Zr facilitate oxygen vacancy formation in CZO(111)? Upon forming an O vacancy, the surface distorts, and two electrons are left localized in two Ce f orbitals, forming polarons.[30,33] Here, a polaron is characterized by electron localization at a Ce site and a radially outward relaxation of O surrounding the site. Therefore, following the formalism of Wang *et al.*,[34] we decompose the oxygen vacancy formation energy (ΔE^{O_v}) into the energy required to remove oxygen from the fixed CZO(111) structure (ΔE^{bond}) and the energy gained from relaxing the atoms upon oxygen removal (ΔE^{strain}). The energies are given by eqn (3) and (4):

Table 2 ΔE^{bond} and ΔE^{strain} values for the single oxygen vacancies

Oxygen atom removed	ΔE^{bond} (eV)	ΔE^{strain} (eV)
O_{Zr}^{sub}	4.07	−2.85
O_{Zr}^{s}	5.08	−3.66
O_{Ce}^{sub}	4.34	−2.53
O_{Ce}^{s}	4.29	−2.22

$$\Delta E^{bond} = E^{O_v\text{-}CZO}_{unrelax} + \frac{1}{2}E_{O_2} - E^{s\text{-}CZO} \quad (3)$$

$$\Delta E^{strain} = E^{O_v\text{-}CZO} - E^{O_v\text{-}CZO}_{unrelax} \quad (4)$$

From Table 2, we see that removing O_{Zr} atoms from the surface and subsurface results in a higher relaxation-induced stabilization compared to O_{Ce} atoms. We evaluate this result

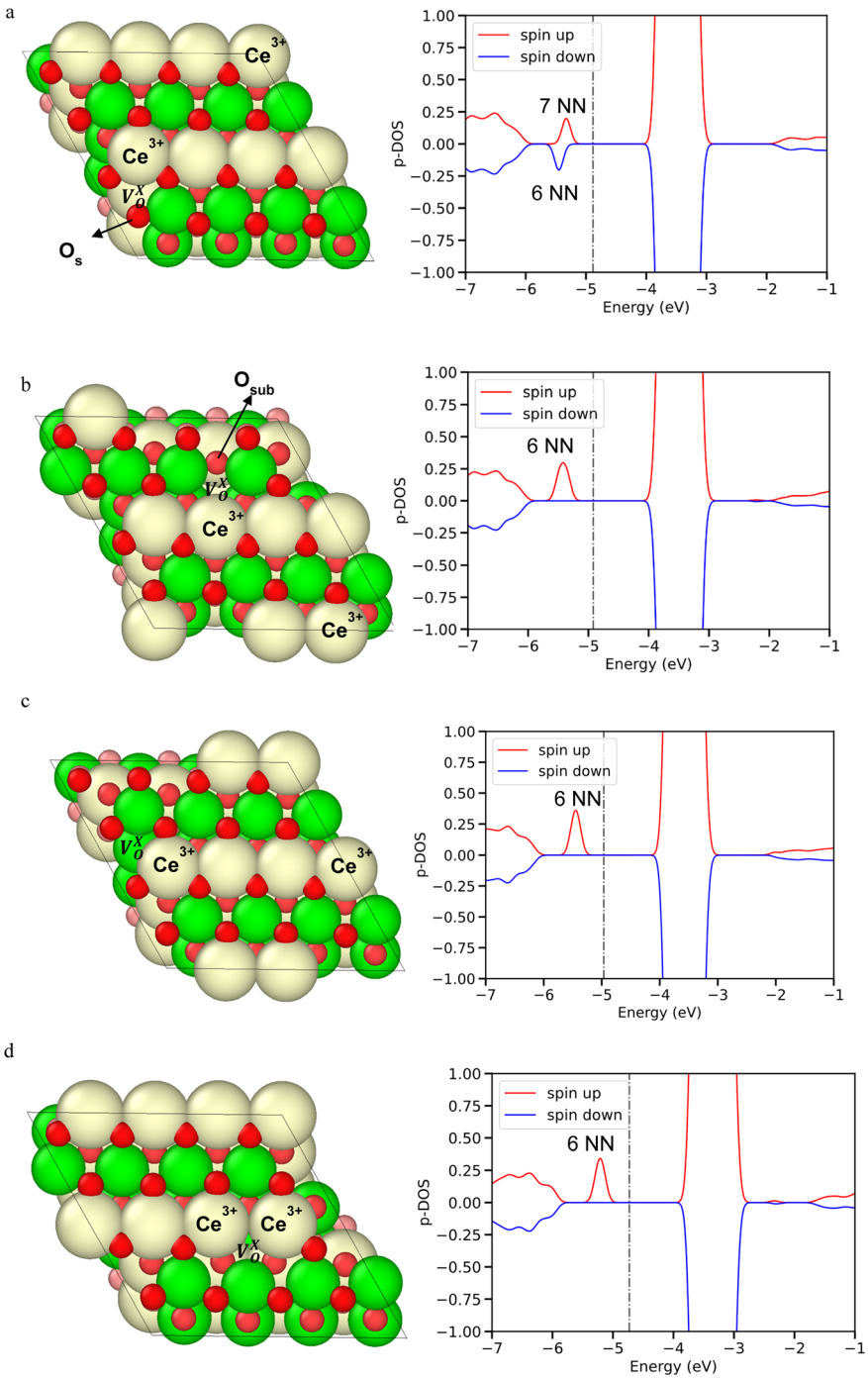

Fig. 2 Defective CZO(111) surface showing the vacancy and reduced cerium atoms and Ce pDOS on its f states for (a) O_{Zr}^{sub} vacancy, (b) O_{Zr}^{s} vacancy, (c) O_{Ce}^{sub} vacancy, and (d) O_{Ce}^{s} vacancy. (O, red; Ce, yellow; Zr, green). Left structures; right pDOS. The vertical gray dashed line indicates the Fermi level referenced to the vacuum level.

with more analysis in the following section. Given the differing coordination environments at the surface and subsurface, we compare surface oxygens only with other surface oxygens and subsurface oxygens only with other subsurface oxygen atoms.

We now turn to electronic and geometric analyses to further understand the role of Zr in stabilizing oxygen vacancy formation. Fig. 2 shows non-stoichiometric CZO(111) surface structures with the single oxygen vacancy and the corresponding projected density of states (pDOS) on the Ce f orbitals. The cerium atoms stabilizing polarons are highlighted. The stability of multiple possible configurations of Ce^{3+} ions around the vacancy is evaluated, following the procedure in Otero *et al.*[31] The peaks just below the Fermi level in the pDOS arise from the reduction of Ce^{4+} to Ce^{3+}. Fig. 2a shows that for the vacancy at O_{Zr}^{sub}, the electrons are localized on dissimilar Ce atoms: one is a 6-coordinated surface atom adjacent to the vacancy and the other is a 7-coordinated surface atom away from the vacancy (although one of the Ce–O bonds is elongated to 2.8 Å, so it is not entirely 7-coordinated). The higher-energy f-orbital belongs to the 7-coordinate Ce^{3+}. This is because the reduction of Ce^{4+} with a higher number of oxygen neighbors weakens the Ce–O ionic bond more. Similarly, for the vacancy at O_{Zr}^{s}, the electrons localize on Ce atoms with a seemingly less pronounced dissimilarity due to both electrons having the same spin; the Ce atom away from the vacancy also has one of its Ce–O bonds elongated to 2.8 Å, making it closer to a 6-fold coordination (Fig. 2b). The vacancies at O_{Ce}^{sub} and O_{Ce}^{s} are accompanied by electron localization on indistinguishable surface Ce atoms, and the f-states are nearly degenerate (Fig. 2c and d). The Ce f orbitals all have similar energies, making it challenging to determine the role of Zr in oxygen vacancy formation. Hence, we turn to geometric analysis to probe the ΔE^{strain} noted above.

Visual inspection reveals significant distortions around the O_{Zr}^{sub} vacancy. The highlighted surface oxygen (Fig. 2a) shifts downward along the surface normal by 0.33 Å. Distortion-based stabilization of oxygen vacancies around Zr ions has been discussed for Zr-doped CeO_2(111) surfaces; however, it has only been quantified in bulk CZO.[35] Here, we compute the root-mean-square of displacements (RMSD) between oxygen atoms in the relaxed and unrelaxed geometry to quantify the extent of surface distortion accompanying vacancy formation eqn (5):[34]

$$\mathrm{RMSD} = \sqrt{\frac{1}{n}\sum_{i=1}^{n}(r_i - r_i^0)^2} \quad (5)$$

where n is the number of oxygen atoms, r_i and r_i^0 are the positions of the oxygen atoms in the relaxed and unrelaxed geometries, respectively. We did not include Ce and Zr in our analysis as they undergo significantly less relaxation than the oxygen atoms. We computed the RMSD of the oxygen atoms in the first coordination shell of the vacancy (Fig. S3†), as these atoms show the most pronounced relaxation. To consider the possibility of relaxation of oxygen atoms further away from the vacancy on the surface, we also computed the RMSD of all the oxygen atoms in the surface and subsurface layers (indicated as 'extended' in Table 3).

Table 3 RMSD between relaxed and unrelaxed structures with the oxygen vacancy. Computations are done for two cases: oxygen atoms in the first coordination shell of the vacancy (first shell) and oxygen atoms in the first coordination shell and on the surface (extended)

RMSD (Å)	O_{Ce}	O_{Zr}
Surface (first shell)	0.28	0.4
Surface (extended)	0.08	0.09
Subsurface (first shell)	0.22	0.25
Subsurface (extended)	0.1	0.1

O_{Zr} vacancies at the surface and subsurface distort the structure more than O_{Ce} vacancy. This agrees with the view of distortion-induced stabilization of oxygen vacancies around Zr atoms previously noted in bulk CZO.[25] Greater structural relaxation upon vacancy formation helps accommodate the larger Ce^{3+} ions in the lattice. Similar ΔE^{strain} trends between O_{Zr} and O_{Ce} vacancies were noted in Table 2, showing that the RMSDs upon vacancy formation correlate with the ΔE^{strain} like in bulk CZO.

All the ΔE^{v} values reported so far have been computed at T = 0 K and μ_O (T = 0 K, p) = 0 and are not representative of vacancy formation under reaction conditions. Therefore, we examine the stability of the defected-CZO(111) surfaces at finite temperatures and different O_2 partial pressures. It is useful to understand vacancy stability under oxidant-rich and oxidant-poor conditions, especially for Mars–van Krevelen reaction mechanisms, which invoke oxidation and reduction half-cycles involving lattice O. Assuming the surface vibrational contribution to the free energy does not affect trends, we write the free energy of vacancy formation as in eqn (6)

$$\Delta G^{v} = E^{v\text{-}CZO} - E^{s\text{-}CZO} + N_v^O\mu_O + N_v^{Ce}\left[e_{CeO_2}^{bulk} - 2\mu_O\right] \text{ when } e_{CeO_2}^{bulk} < e_{Ce_2O_3}^{bulk}$$

or

$$\Delta G^{v} = E^{v\text{-}CZO} - E^{s\text{-}CZO} + N_v^O\mu_O + \frac{N_v^{Ce}}{2}\left[e_{Ce_2O_3}^{bulk} - 3\mu_O\right] \text{ when } {}^{bulk}_{Ce_2O_3} \quad (6)$$
$$< e_{CeO_2}^{bulk}$$

where $E^{v\text{-}CZO}$ is the total energy of the defected CZO slab, N_v^O and N_v^{Ce} are the numbers of O and Ce vacancies, respectively, and $\mu_O(T, p)$ is the chemical potential of atomic oxygen in the reservoir. Here, it is convenient to introduce $\Delta\mu_O$ as μ_O referenced to half the total energy of oxygen in an isolated molecule at 0 K $\left(\Delta\mu_O = \mu_O(T,p) - \frac{1}{2}[E_{O_2}]\right)$. Based on the DFT+U formation energies of the bulk oxides, $\frac{1}{2}\left[e_{Ce_2O_3}^{bulk} - 3\mu_O\right] = e_{CeO_2}^{bulk} - 2\mu_O$ at $\Delta\mu_O$ = −2.12 eV per atom.

Under DRM conditions where lattice O abstraction by CO and O vacancy replenishment by CO_2 are quasi-equilibrated, the effective O chemical potential is defined as: $\mu_O = \mu_{CO_2} - \mu_{CO}$. Here, rather than the partial pressure of O_2, μ_O under reaction conditions depends on the ratio of CO_2 and CO partial pressures. We follow Zhang *et al.*'s methodology to compute the reaction-relevant range,[21] and find that for $T/K \in [800, 1100]$, $\Delta\mu_O(T, p)$/eV per atom $\in [-3.78, -3.03]$. Since $\Delta\mu_O = -3.15$ eV per atom when p_{CO_2}/p_{CO} is 0.5, $\Delta\mu_O$ values between −3.15 and −3.78 eV per atom correspond to increasingly reducing conditions and between −3.15 and −3.03 eV per atom to increasingly oxidizing conditions.

The upper bound of $\mu_O(T, p)$ can be extended to the energy of an isolated O_2 molecule at 0 K, namely

$$\max(\mu_O(T, p)) = \frac{1}{2}[E_{O_2}]$$

Therefore, for $\mu_O(T, p)$ referenced to the energy of an isolated O_2 molecule at 0 K, the bounds are

$$-4 < \mu_O(T, p) - \frac{1}{2}[E_{O_2}] < 0$$

Fig. 3 shows the relative stability of different types of defects on CZO(111). In addition to oxygen and cerium vacancies, we have investigated a cerium vacancy with one oxygen vacancy (Ce_v, O_v) and with two oxygen vacancies (Ce_v, $(O_v)_2$). Under reducing conditions, oxygen vacancy is favored, with a more negative ΔG^v than on $CeO_2(111)$[21] consistent with the reported higher reducibility of CZO.[7] Increasing $\mu_O(T, p)$ favors cerium vacancy creation, but even under strongly oxidizing conditions, an oxygen vacancy is favorable over a cerium vacancy. Overall, under DRM conditions, oxygen vacancies are most likely in the CZO surface. The defect stability trends on the CZO(111) surface resemble $CeO_2(111)$. In the next section, we discuss how Ni single atoms and clusters alter the stability of the vacancies.

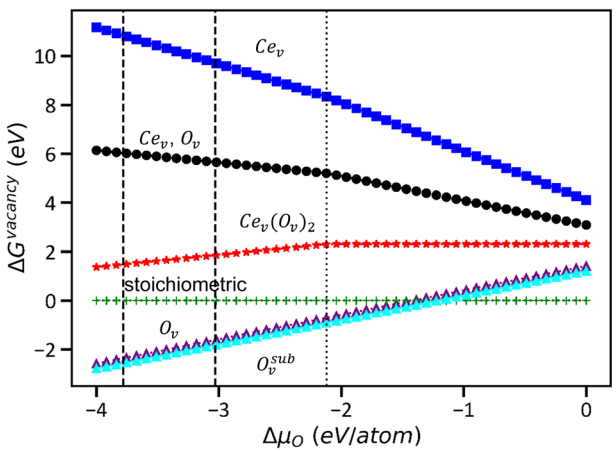

Fig. 3 Vacancy formation energy (ΔG^v) as a function of oxygen chemical potential ($\Delta\mu_O$) with the most stable cerium oxide phase as a reference (bulk CeO_2 and bulk Ce_2O_3 to the right and left, respectively, of the vertical dotted line at $\Delta\mu_O = -2.12$ eV per atom). The left end of the graphs corresponds to reducing conditions, and the right end to oxidizing conditions. The region between the vertical dashed lines ($\Delta\mu_O(T, p) \in [-3.78, -3.03]$) represents typical DRM reaction conditions.

Structure, electronic properties, and stability of Ni anchored on CZO surfaces

While Ni/CZO is an attractive catalyst for DRM, nickel's interactions with the CZO support under reaction conditions remain largely unexplored. In this section, we investigate the stability and electronic properties of Ni and Ni_4 structures on stoichiometric and non-stoichiometric CZO(111) surfaces and how nickel affects support reducibility.

First, we investigate nickel adsorption on the stoichiometric CZO(111) surface. Nickel binding energy on the surface per metal atom $\left(\Delta E_{Ni_n}^{s\text{-}CZO}\right)$ is computed using eqn (7)

$$\Delta E_{Ni_n}^{s\text{-}CZO} = \left(E_{Ni_n}^{s\text{-}CZO} - E^{s\text{-}CZO} - n e_{Ni}^{bulk}\right)/n \quad (7)$$

where $\Delta E_{Ni_n}^{s\text{-}CZO}$ is the total energy of the stoichiometric CZO slab with a Ni_n cluster on it, n is the nuclearity of the Ni cluster, and e_{Ni}^{bulk} is the total energy of bulk nickel per atom. $\Delta E_{Ni_n}^{s\text{-}CZO}$ measures the stability of a Ni_n cluster relative to the bulk: large, positive values indicate a strong preference for Ni to stay in the bulk phase.

We considered six locations to anchor Ni adatoms: atop a Ce atom (Ni_{Ce}), atop a Zr atom (Ni_{Zr}), atop O_{Zr} ($Ni_{O_{Zr}}$), atop O_{Ce} ($Ni_{O_{Ce}}$), the hollow site formed by a Ce and two Zr atoms (Ni_{Zr_2Ce}) and the hollow site formed by a Zr and two Ce atoms (Ni_{Ce_2Zr}) (Fig. S4†). The adsorption energies are shown in Table 4. Ni is most stable at the hollow site formed by a Zr and two Ce atoms (Ni_{Ce_2Zr}). With a $\Delta E_{Ni}^{s\text{-}CZO}$ of 0.04 eV, the nickel adatom is as stable as it would be in the bulk. Interestingly, Ni adsorption on $CeO_2(111)$ has a $\Delta E_{Ni}^{CeO_2}$ of 0.45 eV, which is closer in energy to the Ni_{Zr_2Ce} site. Analysis of the geometries reveals distinct coordination environments. In the Ni_{Ce_2Zr} site, nickel coordinates to two O_{Zr} atoms adjacent to the hollow site in a bridge geometry. The O_{Zr} atoms are significantly displaced by ~0.8 Å out of the plane Fig. 4a). In contrast, at the less stable Ni_{Zr_2Ce} site, nickel adopts a three-fold coordination with the adjacent oxygen atoms (Fig. 4b). Similarly, on $CeO_2(111)$, nickel binds at the hollow site with a three-fold coordination to the surface oxygen atoms, resulting in a binding energy comparable to

Table 4 Nickel binding energy on stoichiometric CZO(111) and $CeO_2(111)$

Binding site	$\Delta E_{Ni}^{s\text{-}CZO}/\Delta E_{Ni}^{CeO_2}$ (wrt e_{Ni}^{bulk}, eV)
Ni_{Ce}	1.51
Ni_{Zr}	1.16
$Ni_{O_{Ce}}$	2.39
$Ni_{O_{Zr}}$	1.99
Ni_{Ce_2Zr}	0.04
Ni_{Zr_2Ce}	0.31
Ni/CeO_2	0.45

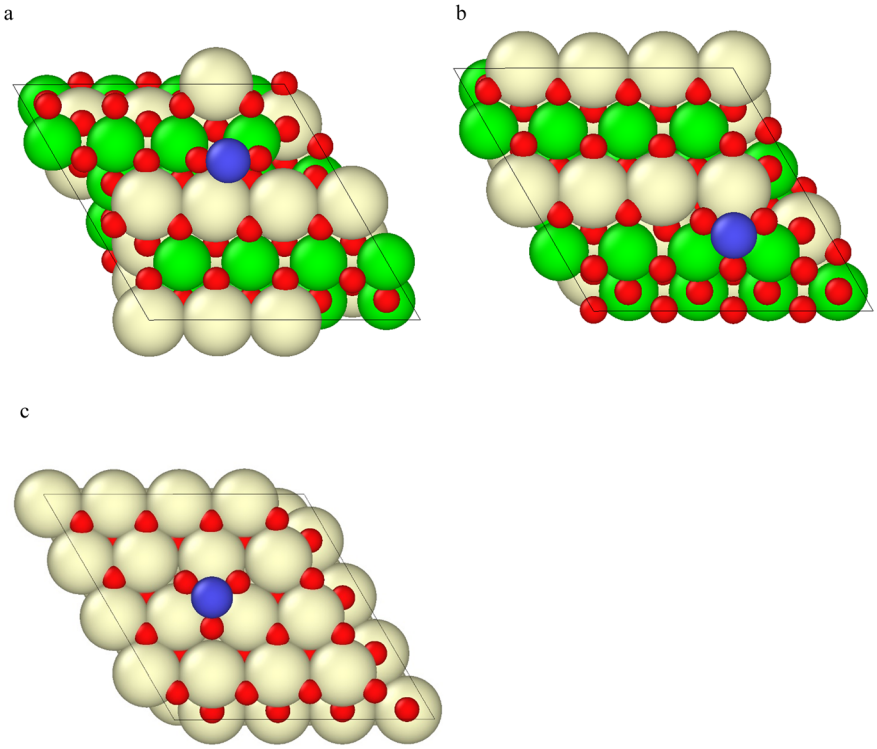

Fig. 4 Nickel binding sites (a) Ni_{Ce_2Zr}/CZO(111), (b) Ni_{Zr_2Ce}/CZO(111) and (c) Ni/CeO_2(111) (O, red; Ce, yellow; Zr, green; Ni, blue).

that of the Ni_{Zr_2Ce} site (Fig. 4c). The notably stronger binding on CZO(111) can be attributed to the substantial structural distortion of the O_{Zr} atoms, which facilitates nickel's bridging mode. Interestingly, Mao *et al.*[36] found that Ni binds to the ⟨110⟩-type step edge of CeO_2(111) in a similar O–Ni–O bridging geometry and is more stable in this configuration than as bulk Ni. This similarity shows the importance of lattice flexibility in creating stable binding sites for single atoms. In summary, the CZO(111) terrace facilitates the dispersion of Ni single atoms much more effectively than the CeO_2(111) terrace.

A similar exploration was carried out to identify the most stable binding geometry of a Ni_4 cluster (Fig. S5†); the top view of the stable structure is shown in Fig. S6.† Mao *et al.*[36] showed that Ni_4 prefers the pyramidal geometry over planar on CeO_2(111). On the CZO surface too, the most stable Ni_4 cluster assumes pyramidal geometry atop a Zr atom. With a $\Delta E_{Ni_4}^{s\text{-}CZO}$ of 0.68 eV, the nickel cluster is less stable at the surface than the adatom. Upon closely inspecting the geometries, we see that the three Ni atoms at the base of the pyramid interact with the surface oxygen atoms and displace them, but by a smaller amount than the single atom. The average Ni–O bond length for the adatom is 1.71 Å, while for the cluster it is 1.79 Å. This indicates that the Ni–O bonding is weaker in the cluster due to competing Ni–Ni bonds, and results in weaker interactions with the support.

Next, we investigate how anchored nickel affects surface reducibility. Unlike Au and Pd, Ni is unstable when anchored to oxygen vacancies, as evidenced by nickel heat of adsorption experiments on CeO_{2-x}(111) surfaces.[36] This instability arises from nickel's pronounced oxophilicity, which favors coordination with oxygen atoms rather than binding to or nucleating at defects. To investigate how nickel affects surface reducibility compared to bare CZO(111), we compute the energetics for oxygen vacancy formation on Ni/CZO(111) and Ni_4/CZO(111) using eqn (8):

$$\Delta E_{Ni_n}^{O_v} = E_{Ni_n}^{O_v} - E_{Ni_n}^{s\text{-}CZO} + \frac{1}{2}E_{O_2} \quad (8)$$

where $E_{Ni_n}^{O_v}$ is the energy of the CZO(111) slab with an oxygen vacancy and a Ni_n cluster on it. We consider surface oxygen vacancies in the same O_{Zr} row (denoted O_{Zr}_NN), as the oxygens coordinated to nickel, and in the adjacent O_{Zr} row (denoted O_{Zr}_NNN). While surface oxygen vacancies are kinetically relevant for the DRM reaction, there is a thermodynamic driving force to create the more stable subsurface oxygen vacancies. At DRM-relevant temperatures of 1000 K, oxygen mobility should allow vacancy diffusion to the subsurface. Therefore, we also evaluated an adjacent subsurface oxygen vacancy formation. Table 5 shows the vacancy formation energies as per eqn (8); Fig. S7 and S8† show the structures.

Table 5 Oxygen vacancy formation energies on Ni_n/CZO

Vacancy formation energy (eV)	Surface	Subsurface
$\Delta E_{Ni}^{O_v}$ – O_{Zr}_NN	1.86	1.85
$\Delta E_{Ni}^{O_v}$ – O_{Zr}_NNN	1.4	1.2
$\Delta E_{Ni_4}^{O_v}$ – O_{Zr}_NN	—	1.35
$\Delta E_{Ni_4}^{O_v}$ – O_{Zr}_NNN	1.7	1.2

ΔE^{O_v} in Table 1 and $\Delta E^{O_v}_{Ni_n}$ in Table 5 indicate that nickel on the CZO(111) surface generally destabilizes O_{Zr} vacancies, especially surface vacancies with larger Ni clusters.

For Ni/CZO, the O_{Zr} vacancy formation energy reduces to that on the pristine surface further away from the Ni single atom. Interestingly, upon optimization, a surface O_{Zr} vacancy near the nickel cluster on Ni_4/CZO converges to the thermodynamically favored subsurface O_{Zr} vacancy, reflecting nickel's high oxophilicity. In addition to the structures in Table 5, we also computed oxygen vacancy formation energy at the foot of the Ni single atom and cluster (denoted O_{Zr}_Ni), as these vacancies may be more kinetically favored. $\Delta E^{O_v}_{Ni} - O_{Zr}$_Ni and $\Delta E^{O_v}_{Ni_4} - O_{Zr}$_Ni are 3.57 eV and 2.7 eV, respectively, further evidencing nickel's high oxophilicity. The destabilization of oxygen vacancies near nickel contrasts with less oxophilic metals, such as Au, which can undergo partial reduction upon interacting with supports like CeO_2 and TiO_2.[37] We next explored the mechanism of O_{Zr} vacancy destabilization. Comparing ΔE^{strain} values in Tables 2 and S3,† we see that O_{Zr} vacancy formation away from the Ni single atom has similar strain effects as the pristine surface. In contrast, the nearest neighbor O_{Zr} vacancy benefits less from structural relaxation effects (Table S3†). These findings indicate that the enhanced performance of the Ni/CZO catalyst for DRM cannot be attributed to the thermodynamics of vacancy formation, as Ni's oxophilicity and the reduced lattice flexibility due to Ni–O bonding destabilizes surrounding O vacancies. Instead, the improvement arises from improved kinetics of breaking H–H or C–H bonds over Ni sites and the subsequent vacancy formation at the Ni/CZO interface.

Under the highly reducing conditions of DRM reaction or the oscillating reducing/oxidizing conditions during CH_4/CO_2 half-cycles of chemical looping DRM, we expect the redox-active CZO surface to be defect-rich. It is then worth checking whether Ni might preferentially bind to surface defects rather than fully oxidized CZO(111) under reaction conditions. Beginning with oxidizing conditions, Jenkins and coworkers[32] have suggested surface Ce vacancies for the Au/CeO_2(111) catalyst in such environments. However, for the Ni/CZO(111) catalyst, Ni cannot assume a Ni^{4+} configuration upon Ce vacancy formation due to unstable dangling bonds on surface oxygen. We, therefore, introduced two oxygen vacancies adjacent to a Ce vacancy ($Ce_v(O_v)_2$), to prevent dangling oxygen bonds. It is worth noting that nickel adsorption at the cerium vacancy is equivalent to Ni^{2+} doping the CZO(111) surface, which favors the creation of two oxygen vacancies for charge compensation. We define the binding energy of nickel to the pristine and $Ce_v(O_v)_2$–CZO surfaces by eqn (9):

$$\Delta E^{Ce_v(O_v)_2-CZO}_{Ni_n} = \left(E^{Ce_v(O_v)_2-CZO}_{Ni_n} - E^{Ce_v(O_v)_2-CZO} - nE^{bulk}_{Ni}\right)/n \quad (9)$$

where $E^{Ce_v(O_v)_2-CZO}_{Ni_n}$ is the energy of the slab with a $Ce_v(O_v)_2$ defect and a Ni_n cluster. In this definition of binding energy, the energy change depends only on Ni adsorption, as defects are expected to be naturally present.[32]

From Table 6, we see that the Ni adatom is very stable at the $Ce_v(O_v)_2$ defect, more so than on the pristine surface. Examination of the geometry (Fig. S9c†) reveals that the Ni adatom forms a stable square-planar complex with two surface and two subsurface oxygens. In contrast, Ni coordinates with two surface oxygen atoms on the pristine surface. This enhanced stability of the Ni adatom on the $Ce_v(O_v)_2$–CZO surface can be attributed to its ability to coordinate with more oxygen atoms than on the pristine surface.

While nickel atoms are highly oxophilic and stabilized by coordinating with oxygens, they can also be stabilized through interactions with other nickel atoms during sintering. We expect this to be the primary mode of Ni stabilization once all Ce vacancies are filled or under reducing reaction conditions. By computing the nucleation energy per Ni atom (ΔE^{s}_{nuc}) from eqn (10), we find that on the pristine surface, the surface with an oxygen vacancy at the O_{Zr}_NNN site, and the $Ce_v(O_v)_2$ defect site, nickel remains dispersed as single atoms. In contrast, Ni single atoms are highly unstable at the oxygen vacancy site. The thermodynamic driving force for nucleation strongly correlates with the number of coordinating oxygen atoms around the nickel adatom: the lowest driving force is observed at the $Ce_v(O_v)_2$ defect site, where Ni coordinates with four oxygens, while the highest is at the oxygen vacancy site, where Ni coordinates with no oxygen atom (Table 7).

$$\Delta E^{s}_{nuc} = \left(E^{s}_{Ni_4} + 3E^{s} - 4E^{s}_{Ni}\right)/4 \quad (10)$$

To understand the electronic origins of the differences in nickel stability across surfaces, we analyze nickel's Bader charges and the number of reduced Ce^{3+} species on the surface. The number of reduced Ce^{3+} species can be related to the extent of surface reduction (as discussed in the previous section of the paper) and consequently, nickel's oxidation state. Due to Ni's oxophilicity, we expect the most strongly adsorbed Ni species to be largely cationic. Table 8 shows the Bader charges on the nickel adatoms and clusters. Nickel remains either cationic or metallic across surfaces. From Table S4,† we note that Ni single atoms have an

Table 6 Nickel binding energy per atom on CZO(111) surfaces

Energy (eV)/defect	s-CZO	$Ce_v(O_v)_2$–CZO
$\Delta E^{surface}_{Ni}$	0.04	−2.4
$\Delta E^{surface}_{Ni_4}$	0.69	0.12

Table 7 Nucleation energy (per Ni atom) across CZO surfaces

Surface	Nucleation energy (ΔE^{s}_{nuc}) in eV
s-CZO	0.65
O_{Zr}_Ni–CZO	−1.18
O_{Zr}_NNN–CZO	0.75
$Ce_v(O_v)_2$–CZO	2.56

Table 8 Electron transfer from nickel (per atom) to the support

Surface	q_{Ni}	q_{Ni_4}
s-CZO	0.7	0.3, 0.3, 0.3, 0
O_{Zr}_Ni–CZO	−0.02	0.15, 0.15, 0.35, 0
O_{Zr}_NN–CZO	0.7	0.3, 0.3, 0.3, 0
O_{Zr}_NNN–CZO	0.7	0.3, 0.3, 0.3, 0
$Ce_v(O_v)_2$–CZO	0.9	0.3, 0.5, 0.7, 0

oxidation state of +2 on the pristine surface and when adsorbed at a CeO_2 vacancy, and remains metallic at an O_{Zr} vacancy. For Ni_4, due to its pyramidal geometry when binding to surface O, the three basal Ni atoms in contact with the surface oxygens exhibit cationic character. In contrast, the apex Ni atom is metallic. When Ni_4 binds to $Ce_v(O_v)_2$ or O_v defects, the basal Ni atoms lose their symmetry, exhibiting varying levels of interaction with the surrounding oxygens. Specifically, on the $Ce_v(O_v)_2$ defect site, one of the Ni atoms adopts a square planar coordination with surface and subsurface oxygens, while the other Ni atoms interact weakly with the oxygens (Fig. S10†). The extent of electron transfer from the nickel adatom to the surface correlates with its resistance to sintering: the highest charge transfer is noted on $Ce_v(O_v)_2$–CZO, which stabilizes the adatom the most, followed by the pristine surface and the surfaces with the oxygen vacancy at the O_{Zr}_NN and O_{Zr}_NNN positions. Nickel remains metallic on O_{Zr}_Ni–CZO, which explains why sintering or diffusion to sites with oxygen atoms could be favorable at DRM temperatures.

Oxygen vacancies adjacent to nickel, while kinetically relevant, are energetically unfavorable due to nickel's pronounced oxophilicity. Nevertheless, understanding the stability of such surface defects adjacent to nickel under realistic oxygen partial pressures is crucial for elucidating the catalytic behavior of Ni/CZO systems. Therefore, we plot $\Delta G_{Ni_n}^{v\text{-}CZO}$ (defined below) as a function of μ_O (Fig. 5), in the spirit of the analysis presented in Fig. 3. This definition of $\Delta G_{Ni_n}^{v\text{-}CZO}$ computes the Ni binding energy to the non-stoichiometric surface but also includes a correction for the formation of the defect, as given in eqn (11).

$$\Delta G_{Ni_n}^{v\text{-}CZO} = \left(E_{Ni_n}^{v\text{-}CZO} - E^{s\text{-}CZO} + N_v^O\mu_O + N_v^{Ce}\left[e_{CeO_2}^{bulk} - 2\mu_O\right] - nE_{Ni_{bulk}}\right)/ne_{CeO_2}^{bulk} < e_{Ce_2O_3}^{bulk}$$

or

$$\Delta G_{Ni_n}^{v\text{-}CZO} = \left(E_{Ni_n}^{v\text{-}CZO} - E^{s\text{-}CZO} + N_v^O\mu_O + \frac{N_v^{Ce}}{2}\left[e_{CeO_2}^{bulk} - 3\mu_O\right] - nE_{Ni_{bulk}}\right)/ne_{Ce_2O_3}^{bulk} < e_{CeO_2}^{bulk} \quad (11)$$

Fig. 5 shows that across the $\Delta\mu_O(T, p)$ range, oxygen vacancies further away from nickel are most favorable due to nickel adatoms and clusters coordinating with oxygen atoms. Such sites may not occur under reducing conditions with a high concentration of oxygen vacancies. Therefore, we consider other defects that stabilize nickel. In the DRM-relevant range of $\Delta\mu_O(T, p)$/eV per atom $\in$ [−3.78, −3.03], Ni single atoms stabilize $Ce_v(O_v)_2$ defect sites, which are unfavorable on the pristine CZO surface. The Ni_4 cluster, on the other hand, can bind favorably at the surface oxygen vacancy and the $Ce_v(O_v)_2$ defect site under DRM-relevant conditions. Overall, comparison with Fig. 3 shows that the nickel stabilizes Ce_v, the pair of O_v and Ce_v, and $Ce_v(O_v)_2$ formation.

Conclusions

We employed DFT and *ab initio* thermodynamics to investigate the energetics, stability, and electronic properties of vacancy formation and nickel adsorption on CZO(111). Subsurface and surface oxygen vacancies are favored near Zr^{4+} ions due to distortion-induced stabilization, and the latter are more favorable across DRM-relevant conditions. Ni single atoms coordinate with two O_{Zr} surface atoms as Ni^{2+} motifs, unlike three-fold coordinated Ni atoms on hollow sites of CeO_2(111). Interestingly, Ni dislikes direct binding to oxygen vacancies compared to a pristine surface due to its oxophilicity as well as electrostatic repulsion from multiple surface Ce^{3+} ions. The enhanced performance of the Ni/CZO

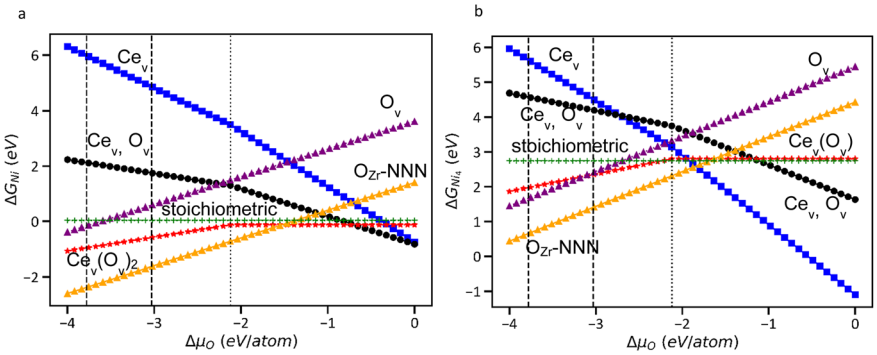

Fig. 5 Nickel (a) single atom and (b) cluster (Ni_4) adsorption energy on the defected and pristine-CZO surfaces as a function of oxygen chemical potential (μ_O). The most stable cerium oxide phase is used as reference (bulk Ce_2O_3 and bulk CeO_2 to the left and right, respectively, of the vertical dotted line at $\Delta\mu_O$ = −2.12 eV). The left end of the graphs corresponds to reducing conditions, and the right end to oxidizing conditions. The region between the two vertical dashed lines ($\Delta\mu_O(T, p) \in$ [−3.78, −3.03]) represents the typical DRM reaction conditions.

DRM catalyst stems probably from the kinetics of H–H or C–H bond activation, vacancy formation, or oxygen diffusion rather than thermodynamics. Further work is needed to delineate the mechanisms.

Ni adatoms are more stable than Ni_4 at trimer defects comprising one Ce and two oxygen vacancies ($Ce_v(O_v)_2$), at the pristine surface, and at the Ni_{Ce_2Zr} site with a next-nearest neighbor oxygen vacancy due to coordinating with more oxygen atoms. Thus, defects exposing oxygen atoms, *e.g.*, ($Ce_v(O_v)_2$), will stabilize Ni single atoms, but single oxygen surface vacancies would not directly bind Ni_1. Clusters, on the other hand, can bind favorably at a surface oxygen vacancy due to Ni–Ni interactions compensating for the missing surface oxygen. We expect that high Ni loadings will lead to Ni_1 adatoms anchoring next to oxygen vacancies, divacancies, and pristine areas and Ni clusters stabilized by oxygen vacancies at their perimetry or underneath. The extent of electron transfer from the metal to the surface and, thus, the degree of cationic character of a nickel adatom will vary with its location and defect type and correlate positively with its resistance to sintering: the highest charge transfer is on $Ce_v(O_v)_2$, followed by the pristine surface and surfaces with a single oxygen vacancy in the next nearest neighbor position. In an actual catalyst, we thus expect Ni atoms with varying metallic character and nuclearity to participate in the chemistry.

These findings provide valuable insights into the Ni/CZO DRM catalysts, emphasizing the importance of nickel's electronic interactions with defect sites of the CZO surface.

Data availability

The data supporting this article have been included as part of the ESI.†

Conflicts of interest

There are no conflicts of interest to declare.

Acknowledgements

This work was supported by the US Department of Energy (DOE), award number DE-SC0024085. The computations were partially supported by the high-performance computing resources at the University of Delaware. The authors thank Dr. Jeffrey Frey and Rajas Mehendale for installing the software on the high-performance computing cluster. The authors are grateful to Dr. Stavros Caratzoulas, who sadly passed away while preparing this work.

References

1 Q. Wang, X. Chen, A. N. Jha and H. Rogers, Natural gas from shale formation – The evolution, evidences and challenges of shale gas revolution in United States, *Renewable Sustainable Energy Rev.*, 2014, **30**, 1–28.
2 H. Ishaq, I. Dincer and C. Crawford, A review on hydrogen production and utilization: Challenges and opportunities, *Int. J. Hydrogen Energy*, 2022, **47**(62), 26238–26264.
3 O. J. Guerra, J. Eichman, J. Kurtz and B.-M. Hodge, Cost Competitiveness of Electrolytic Hydrogen, *Joule*, 2019, **3**(10), 2425–2443.
4 C. Wang, S. Sourav, K. Yu, Y. Kwak, W. Zheng and D. G. Vlachos, Green Syngas Production by Microwave-Assisted Dry Reforming of Methane on Doped Ceria Catalysts, *ACS Sustainable Chem. Eng.*, 2023, **11**(36), 13353–13362.
5 Z. Liu, D. C. Grinter, P. G. Lustemberg, T.-D. Nguyen-Phan, Y. Zhou, S. Luo, I. Waluyo, E. J. Crumlin, D. J. Stacchiola, J. Zhou, J. Carrasco, H. F. Busnengo, M. V. Ganduglia-Pirovano, S. D. Senanayake and J. A. Rodriguez, Dry Reforming of Methane on a Highly-Active Ni-CeO2 Catalyst: Effects of Metal-Support Interactions on C–H Bond Breaking, *Angew. Chem., Int. Ed.*, 2016, **55**(26), 7455–7459.
6 Z. Yang, T. K. Woo and K. Hermansson, Effects of Zr doping on stoichiometric and reduced ceria: A first-principles study, *J. Chem. Phys.*, 2006, **124**(22), 224704.
7 H.-F. Wang, H.-Y. Li, X.-Q. Gong, Y.-L. Guo, G.-Z. Lu and P. Hu, Oxygen vacancy formation in CeO2 and Ce1−xZrxO2 solid solutions: electron localization, electrostatic potential and structural relaxation, *Phys. Chem. Chem. Phys.*, 2012, **14**(48), 16521–16535.
8 Y. Nagai, T. Yamamoto, T. Tanaka, S. Yoshida, T. Nonaka, T. Okamoto, A. Suda and M. Sugiura, X-ray absorption fine structure analysis of local structure of CeO2–ZrO2 mixed oxides with the same composition ratio (Ce/Zr=1), *Catal. Today*, 2002, **74**(3), 225–234.
9 F. Zhang, Z. Liu, X. Chen, N. Rui, L. E. Betancourt, L. Lin, W. Xu, C.-j. Sun, A. M. M. Abeykoon, J. A. Rodriguez, J. Teržan, K. Lorber, P. Djinović and S. D. Senanayake, Effects of Zr Doping into Ceria for the Dry Reforming of Methane over Ni/CeZrO2 Catalysts: In Situ Studies with XRD, XAFS, and AP-XPS, *ACS Catal.*, 2020, **10**(5), 3274–3284.
10 A. Kambolis, H. Matralis, A. Trovarelli and C. Papadopoulou, Ni/CeO2-ZrO2 catalysts for the dry reforming of methane, *Appl. Catal., A*, 2010, **377**(1), 16–26.
11 S. Xu and X. Wang, Highly active and coking resistant Ni/CeO2–ZrO2 catalyst for partial oxidation of methane, *Fuel*, 2005, **84**(5), 563–567.
12 G. S. Parkinson, Single-Atom Catalysis: How Structure Influences Catalytic Performance, *Catal. Lett.*, 2019, **149**(5), 1137–1146.
13 C. Freysoldt, B. Grabowski, T. Hickel, J. Neugebauer, G. Kresse, A. Janotti and C. G. Van de Walle, First-principles calculations for point defects in solids, *Rev. Mod. Phys.*, 2014, **86**(1), 253–305.
14 G. Kresse and J. Hafner, Ab initio molecular-dynamics simulation of the liquid-metal–amorphous-semiconductor transition in germanium, *Phys. Rev. B: Condens. Matter Mater. Phys.*, 1994, **49**(20), 14251–14269.
15 G. Kresse and J. Furthmüller, Efficiency of ab-initio total energy calculations for metals and semiconductors using a plane-wave basis set, *Comput. Mater. Sci.*, 1996, **6**(1), 15–50.

16 J. P. Perdew, K. Burke and M. Ernzerhof, Generalized Gradient Approximation Made Simple [Phys. Rev. Lett. 77, 3865 (1996)], *Phys. Rev. Lett.*, 1997, **78**(7), 1396–1396.
17 P. E. Blöchl, Projector augmented-wave method, *Phys. Rev. B: Condens. Matter Mater. Phys.*, 1994, **50**(24), 17953–17979.
18 G. Kresse and D. Joubert, From ultrasoft pseudopotentials to the projector augmented-wave method, *Phys. Rev. B: Condens. Matter Mater. Phys.*, 1999, **59**(3), 1758–1775.
19 V. I. Anisimov, J. Zaanen and O. K. Andersen, Band theory and Mott insulators: Hubbard U instead of Stoner I, *Phys. Rev. B: Condens. Matter Mater. Phys.*, 1991, **44**(3), 943–954.
20 A. Rohrbach, J. Hafner and G. Kresse, Electronic correlation effects in transition-metal sulfides, *J. Phys.: Condens. Matter*, 2003, **15**(6), 979.
21 C. Zhang, A. Michaelides, D. A. King and S. J. Jenkins, Anchoring Sites for Initial Au Nucleation on CeO2{111}: O Vacancy versus Ce Vacancy, *J. Phys. Chem. C*, 2009, **113**(16), 6411–6417.
22 H.-Y. T. Chen, S. Tosoni and G. Pacchioni, Adsorption of Ruthenium Atoms and Clusters on Anatase TiO2 and Tetragonal ZrO2(101) Surfaces: A Comparative DFT Study, *J. Phys. Chem. C*, 2015, **119**(20), 10856–10868.
23 S. Livraghi, M. C. Paganini, E. Giamello, G. Di Liberto, S. Tosoni and G. Pacchioni, Formation of Reversible Adducts by Adsorption of Oxygen on Ce–ZrO2: An Unusual η2 Ionic Superoxide, *J. Phys. Chem. C*, 2019, **123**(44), 27088–27096.
24 G. E. Murgida, V. Ferrari, M. V. Ganduglia-Pirovano and A. M. Llois, Ordering of oxygen vacancies and excess charge localization in bulk ceria: A $\mathrm{DFT}+U$ study, *Phys. Rev. B: Condens. Matter Mater. Phys.*, 2014, **90**(11), 115120.
25 H.-F. Wang, Y.-L. Guo, G.-Z. Lu and P. Hu, Maximizing the Localized Relaxation: The Origin of the Outstanding Oxygen Storage Capacity of κ-Ce2Zr2O8, *Angew. Chem., Int. Ed.*, 2009, **48**(44), 8289–8292.
26 Y. Peng, X.-L. Si, C. Shang and Z.-P. Liu, Abundance of Low-Energy Oxygen Vacancy Pairs Dictates the Catalytic Performance of Cerium-Stabilized Zirconia, *J. Am. Chem. Soc.*, 2024, **146**(15), 10822–10832.
27 P. Fornasiero, E. Fonda, R. Di Monte, G. Vlaic, J. Kašpar and M. Graziani, Relationships between Structural/Textural Properties and Redox Behavior in Ce0.6Zr0.4O2 Mixed Oxides, *J. Catal.*, 1999, **187**(1), 177–185.
28 J. C. Conesa, Computer Modeling of Local Level Structures in (Ce, Zr) Mixed Oxide, *J. Phys. Chem. B*, 2003, **107**(34), 8840–8853.
29 M. Nolan, J. E. Fearon and G. W. Watson, Oxygen vacancy formation and migration in ceria, *Solid State Ionics*, 2006, **177**(35), 3069–3074.
30 J. Paier, C. Penschke and J. Sauer, Oxygen Defects and Surface Chemistry of Ceria: Quantum Chemical Studies Compared to Experiment, *Chem. Rev.*, 2013, **113**(6), 3949–3985.
31 G. S. Otero, P. G. Lustemberg, F. Prado and M. V. Ganduglia-Pirovano, Relative Stability of Near-Surface Oxygen Vacancies at the CeO2(111) Surface upon Zirconium Doping, *J. Phys. Chem. C*, 2020, **124**(1), 625–638.
32 C. J. Owen and S. J. Jenkins, Comparative study of single-atom gold and iridium on CeO2{111}, *J. Chem. Phys.*, 2021, **154**(16), 164703.
33 D. García Pintos, A. Juan and B. Irigoyen, Oxygen vacancy formation on the Ni/Ce0.75Zr0.25O2(111) surface. A DFT+U study, *Int. J. Hydrogen Energy*, 2012, **37**(19), 14937–14944.
34 H.-F. Wang, X.-Q. Gong, Y.-L. Guo, Y. Guo, G. Z. Lu and P. Hu, A Model to Understand the Oxygen Vacancy Formation in Zr-Doped CeO2: Electrostatic Interaction and Structural Relaxation, *J. Phys. Chem. C*, 2009, **113**(23), 10229–10232.
35 Z. Yang, Y. Wei, Z. Fu, Z. Lu and K. Hermansson, Facilitated vacancy formation at Zr-doped ceria(111) surfaces, *Surf. Sci.*, 2008, **602**(6), 1199–1206.
36 Z. Mao, P. G. Lustemberg, J. R. Rumptz, M. V. Ganduglia-Pirovano and C. T. Campbell, Ni Nanoparticles on CeO2(111): Energetics, Electron Transfer, and Structure by Ni Adsorption Calorimetry, Spectroscopies, and Density Functional Theory, *ACS Catal.*, 2020, **10**(9), 5101–5114.
37 A. Ruiz Puigdollers, P. Schlexer, S. Tosoni and G. Pacchioni, Increasing Oxide Reducibility: The Role of Metal/Oxide Interfaces in the Formation of Oxygen Vacancies, *ACS Catal.*, 2017, **7**(10), 6493–6513.

